X-RAY CONSTRAINTS ON THE INTERGALACTIC MEDIUM

Thomas Aldcroft, Martin Elvis, Jonathan McDowell, and Fabrizio Fiore[1]
Harvard-Smithsonian Center for Astrophysics, 60 Garden Street, Cambridge, MA 02138

Received ________________; accepted ________________

[1]Present address: Osservatorio Astronomico di Roma via dell'Osservatorio, 5. Monteporzio-Catone (Rm), I00040 Italy

ABSTRACT

We use ROSAT PSPC spectra of $z \approx 3$ quasars to constrain the density and temperature of the intergalactic medium (IGM). Strong low energy cut-offs in PSPC spectra of high-redshift quasars are common. However, the absence of absorption toward some high-redshift quasars can be used to put limits on the possible cosmological density, Ω_G, of a hot diffuse IGM, via an X-ray 'Gunn-Peterson' test using edge and line opacity in the soft X-rays. The K-edges of oxygen, neon, and carbon and the L-edge of iron produce most of the absorption which is spread out by the redshift of the source. We assume an isotropic, isothermal, non-evolving model of the IGM and calculate the optical depth of this absorption. We find that this test can constrain an enriched IGM at temperatures near 10^5 - 10^6 K, intermediate between the hot IGM ruled out by COBE, and the cold IGM ruled out by the traditional Ly-α Gunn-Peterson test. Photoionization of the IGM by the ultraviolet and X-ray background has a large effect. We give results for three $z \approx 3$ quasars and discuss how the various trade-offs among temperature, abundance and background radiation strength affect the limits on Ω_G. In addition to the high-redshift case, we discuss techniques for constraining the IGM using X-ray spectra of low-redshift quasars ($z \approx 0.1 - 0.3$). Currently available X-ray spectral data have insufficient energy resolution to constrain the IGM unambiguously, and so expected detection limits for future high-resolution spectrometers are presented. We find that with a large effective area ($\sim 2000\,\mathrm{cm}^2$) it is possible to substantially constrain or detect the IGM at the densities which are typically predicted.

Subject headings: intergalactic medium — X-rays — quasars : absorption

1. Introduction

For some time there has been indirect evidence which indicates the existence of a diffuse intergalactic medium (IGM). The most compelling pieces of observational evidence are the detection of X-ray emitting gas in galaxy clusters, and the Ly-α forest clouds which are seen in the spectra of high redshift QSOs. Both of these are a direct demonstration that a significant amount of matter exists in the universe which is not condensed into galaxies. In both cases as well, plausible theoretical models explaining the phenomena would point to the existence of an IGM. In the case of the cluster gas, it is found that the gas is highly enriched, and one possible mechanism explaining this is the ejection of processed gas by supernova explosions (e.g. Sarazin 1988). The same process could take place in non-cluster galaxies, which would return the enriched gas to the IGM. In fact, recent numerical simulations of CDM cosmological models find that feedback of energy due to supernovae in forming galaxies can successfully reionize the IGM (Cen & Ostriker 1993 (CO93); Shapiro et al. 1994) (SGB). CO93 find that this energy in the form of galactic superwinds can produce a "warm" IGM by heating over 30% of the intergalactic material to temperatures of 10^5 - 10^6 K. In the case of the Ly-α forest clouds, one of the most natural models which explains their stability relies on pressure confinement from a hot diffuse IGM (Sargent 1988 and references therein).

Other theoretical evidence for an IGM comes from studies of galaxy formation, which generally predict that a significant fraction of the baryonic mass in the universe should remain in the form of a diffuse IGM (Ikeuchi & Ostriker 1986; Shapiro 1989; CO93; SGB). For example, the numerical simulations of SGB reveal that at the very least 20% of the initial baryonic mass is left in the IGM after the epoch of galaxy formation, and for reasonable reionization schemes the fraction is 50 - 90%. The simulations of SGB and CO93 both imply an IGM density in the neighborhood of $\Omega_G \approx 0.02$ and temperature $T \approx 10^5 - 10^7$ K.

Despite the evidence that a diffuse IGM should exist, there still has been no direct detection, nor have the basic properties of this medium such as temperature, density, and chemical composition been strongly constrained. Early efforts to detect the IGM or constrain its properties are summarized in Shapiro & Bahcall (1982) (SB). The most sensitive tests to date are the high temperature limit based on the distortion of the cosmic microwave background spectrum (the Compton y parameter) as measured by the COBE satellite (Mather et al. 1993), and the low temperature limit based on the Ly-α Gunn-Peterson test (Giallongo, Cristiani, & Trevese 1992; Gunn & Peterson 1965). The latter test is based on the fact that neutral hydrogen in the IGM can cause absorption in the spectrum of a QSO blueward of the Ly-α emission line. The limit on absorption optical depth is converted into a constraint on the temperature and density of the IGM by determining the neutral hydrogen fraction, assuming ionization equilibrium. The COBE and Ly-α Gunn-Peterson limits are shown in Fig. 1. We also show for comparison the limit on density based on the standard model of big bang nucleosynthesis $\Omega_B < 0.026h_{100}^{-2}$ (Kolb & Turner 1990), as well as the predicted temperature and density of the IGM based on the simulation of CO93. Finally, we show the best fit values for the IGM if the X-ray background were entirely due to thermal free-free emission in a hot IGM (Field & Perrenod 1977). These values are excluded by the COBE limit. We see that the there is a large range of temperature and density which is unconstrained by the current tests. In particular, the interesting region with $T \approx 10^5 - 10^6$ K and IGM density $\Omega_G \approx 0.01 - 0.1$ has not been probed.

It was realized when quasars were detected in the X-ray band that a Gunn-Peterson test using the X-ray transitions in heavy elements might constrain the IGM at higher temperatures than the original Ly-α Gunn-Peterson test (SB; Sherman & Silk 1979; Sherman 1979). These transitions occur even in the highly ionized species which dominate in plasmas at temperatures between 10^4 to 10^8 K. SB calculated the total absorption optical depth to X-rays due to line and edge transitions and found substantial absorption for high redshift sources over a wide range of interesting temperatures and densities. However, their calculations did not include the effect of the ionizing background radiation which is now known to exist. We find that this radiation strongly affects the ionization equilibrium and can significantly lower the X-ray opacity of the IGM.

In addition to theoretical advances, the quasar X-ray spectra which were available at the time of SB were inadequate to usefully apply their calculations, both because there were too few counts and the energy resolution was too low. The ROSAT mission (Trümper 1983) now provides an opportunity to set limits on the IGM because its high sensitivity in the soft X-ray range allows high redshift quasars to be detected down to ~ 0.1 keV (observed frame). Moreover, the Position Sensitive Proportional Counter (PSPC, Pfefferman et al. 1987) has sufficient spectral resolution to allow several parameter fits for spectra containing a few hundred counts (see e.g. Fiore et al. 1993). High signal-to-noise observations of high-redshift quasars with the ROSAT PSPC have revealed that some of these quasars can be well fitted in the soft X-ray band with only a single power-law and Galactic absorption. This lack of observed X-ray absorption in the IGM can be used to constrain the temperature, density, and heavy-element abundance of the IGM.

In this paper we explore the limits which can be placed on the IGM using the X-ray Gunn-Peterson test at high redshift ($z \approx 3$) and at low redshift ($z \lesssim 0.4$). In Section 2. we explain the calculational details and assumptions used for determining the X-ray optical depth due to the IGM out to a certain redshift, at a particular temperature and density. In Section 3. we use ROSAT PSPC spectra of three high-redshift quasars to set observational constraints on the IGM. Section 4. discusses detection limits for the IGM using high-energy-resolution ($E/\Delta E \gtrsim 100$) observations of low-redshift quasars.

2. X-ray opacity of IGM

The total absorption optical depth due to a column of intergalactic material out to a quasar redshift z_q is calculated by summing the optical depth of each small pathlength to the quasar. Since the contribution from each pathlength is effectively redshifted (because the transmitted photons are redshifted), summing the parts amounts to smearing the rest-frame optical depth over frequency. The equation describing this is

$$\tau_\nu = \int_0^{z_q} \kappa_\nu(z)\big|_{\nu(1+z)} \frac{dl}{dz} dz. \tag{1}$$

where $\kappa_\nu(z)$ is the gas opacity of material at redshift z, evaluated at the frequency $\nu(1+z)$, and $dl/dz = cH_0^{-1}(1+z)^{-2}(1+\Omega_0 z)^{-1/2}$ for the standard Friedmann cosmology. The opacity $\kappa_\nu(z)$ is a function of the gas density, the element abundances, and the ionization state of the elements at each redshift. If we make the assumption that ionization equilibrium holds (discussed in Section 2.5.), then the ionization state is determined by the element abundances, the gas temperature and density, and the ionizing background radiation.

We now discuss in Sections 2.1.-2.5. the assumptions and calculational details which enter into evaluating Equation 1.

2.1. Physical model of IGM

Because very little is known about the physical conditions of the IGM, in our calculations we adopt a model with the simplest possible assumptions: the IGM is isotropic, with density $n(z) = n_0(1+z)^3$; and the heavy element abundances $A(Z)$ (relative to hydrogen, for atomic element Z) and temperature T are independent of redshift. These conditions correspond to isothermal, no-evolution expansion of the IGM. The approximation that the IGM expands isothermally is more accurate than one might initially suppose, according to the simulations of CO93. They find that the energy input from supernova superwinds keeps the IGM temperature in the range $10^5 - 10^6$ K after $z \approx 4$. For the heavy element abundances $A(Z)$ we consider only two possibilities, that of uniform depletion from the "cosmic" abundances of Cameron (1973), and that of a primordial composition with negligible heavy elements. In subsequent discussion, we denote the heavy element abundance by m, where m is the numerical value of the depletion. In the case of primordial abundances, we use $m = 0$. Note that all of the calculations are done for two values of the total mass density, $\Omega_0 = 0.2$ and $\Omega_0 = 1$, with Hubble constant $H_0 = 75$ km s^{-1} Mpc^{-1} (or $h_{100} = 0.75$) throughout.

2.2. Background radiation

Because of the very low particle densities ($n \approx 10^{-6}\,\mathrm{cm}^{-3}$ for $\Omega_G = 1$) in models of the IGM, the ionizing background radiation can be an important factor in determining the ionization equilibrium. Since we are interested in the equilibrium of highly ionized heavy elements, we need an estimate of the background radiation spectrum covering the UV to soft X-ray energy band.

The UV background radiation is best measured by means of the Ly-α proximity effect, which is the observed decrease in the density of Ly-α forest clouds near the QSO redshift (Bechtold 1994; Fall & Pei 1993; Bajtlik, Duncan & Ostriker 1988; Bechtold et al. 1988; Murdoch et al. 1986). The UV background radiation determined by this method is generally taken to have the power-law form

$$J_\nu(z) = 10^{-21} J_{21} \left(\frac{1+z}{1+z_q}\right)^{\beta} \left(\frac{\nu}{\nu_{LL}}\right)^{-\alpha} \mathrm{erg\,s^{-1}\,cm^{-2}\,Hz^{-1}\,sr^{-1}}. \tag{2}$$

Here J_{21} is the dimensionless strength, z_q is the redshift at which the proximity effect is observed, ν_{LL} is the frequency at the hydrogen Lyman limit, and β characterizes the redshift evolution. Based on the range of parameter values found in the literature (which are generally in rough agreement but often formally inconsistent), we use the values $\beta = 4$, $\alpha = 1.5$, and $z_q = 2.5$. The strength J_{21} of the background radiation is uncertain by about a factor of 10, so we do all calculations for two values, $J_{21} = 1.0$ and $J_{21} = 0.1$. An evolution of the background in which $\beta = 3 - 5$ for $z < 2$ (Stanek 1992; Ikeuchi & Turner 1991) and $J_\nu(z)$ is constant for $z > 2$ is probably more realistic; however, in these scenarios the radiation strength differs from the value we have used by less than about a factor of 5. This is comparable to the uncertainty in the radiation strength itself and so our conclusions would be unchanged if we used this evolution.

The soft X-ray background radiation has been directly measured in the range 0.5 to 3.5 keV by Wu et al. (1991) using the Einstein Observatory IPC, and in the range 0.1 to 2.4 keV by Hasinger et al. (1991) with the ROSAT PSPC. These measurements are at zero redshift, so in our calculations we have assumed the same redshift evolution as the UV background, namely $J_\nu(z) \propto (1+z)^4$. Connecting the UV and soft X-ray components together by power-law extrapolation gives the ionizing background which we use in calculating the ionization equilibrium. Note that the relative normalization of the components of the background spectrum is determined for $J_{21} = 1.0$, and stays *fixed* for different values of J_{21}. This means the entire spectrum is scaled, not just the UV component.

2.3. Contributions to opacity

The dominant processes contributing to the opacity k_ν in Equation 1 are atomic line transitions, bound-free (continuum) transitions, and electron Compton scattering. For our purposes the latter process can be ignored because for photon energies much less than 500 keV the cross-section is independent of energy. This means the absorption is not detectable without a priori knowledge of the intrinsic quasar luminosity.

Following the discussion in SB, the opacity due to an atomic line transition in a particular ion of an element can be written

$$\kappa_\nu^{line} = n_{abs}\frac{\pi e^2}{m_e c} f_{12}\delta(\nu - \nu_\alpha),$$

where n_{abs} is the density of the ion, f_{12} is the oscillator strength of the transition, ν_α is the transition frequency, and $\delta(x)$ is the Dirac delta function with $\int \delta(x)dx = 1$. If we insert this formula into Equation 1 we get the result

$$\begin{aligned} \tau_\nu^{line} &= 0.94\left(\frac{1\,\mathrm{keV}}{E_\alpha}\right) f_{12}\,\Omega_G \left(\frac{A(Z)}{10^{-4}}\right) y(Z,\xi)\left(\frac{\nu_\alpha}{\nu}\right)^2 \left(1-\Omega_0+\Omega_0\frac{\nu_\alpha}{\nu}\right)^{-1/2} \\ &\qquad \text{for } \nu_\alpha(1+z)^{-1} \le \nu \le \nu_\alpha \\ &= 0 \qquad \text{for } \nu < \nu_\alpha(1+z)^{-1} \text{ or } \nu > \nu_\alpha \end{aligned} \tag{3}$$

where E_α is the line energy, Ω_G is the fraction of the critical density in the IGM, and $y(Z,\xi)$ is the normalized population of the ionic level ξ. To calculate the total optical depth due to lines, we use Equation 3, with the ion populations $y(Z,\xi)$ determined by the CLOUDY program (Ferland 1993) and the oscillator strengths and line energies as given in Kato (1976).

The continuum or edge opacity due to photoionization can be approximated by

$$\begin{aligned} \kappa_\nu^{edge} &= n_{abs}\sigma_{th}(\nu_{th}/\nu)^3 \quad (\nu \ge \nu_{th}) \\ &= 0 \qquad\qquad\qquad (\nu < \nu_{th}) \end{aligned} \tag{4}$$

where ν_{th} is the frequency of the photoionization threshold and σ_{th} is the cross-section at the threshold. In theory we can sum the opacity from Equation 4 for all the elements and ions, but in practice this is done automatically by CLOUDY and we simply insert the total opacity returned by CLOUDY into Equation 1.

2.4. CLOUDY

To evaluate the opacity and ionization equilibrium as a function of redshift Equation 1, we use the CLOUDY program. The temperature of the gas is fixed and no attempt is made to balance heating and cooling. Instead, the gas is assumed to be heated by some unspecified mechanism to the given temperature. One means for this heating could be shocks from supernova-driven superwinds (e.g. SGB; CO93). Note that the ionizing background radiation alone is insufficient to heat the gas to the temperatures we are considering (Miralda-Escoudé & Rees 1994).

The parameters which we input to CLOUDY for calculating the opacity and ionization state are the density, temperature, abundances, and background radiation. We can reduce the total number of calculations required to constrain the IGM properties by taking advantage of the homology relation which applies for particle densities $n \lesssim 10^3\,\mathrm{cm}^{-3}$,

$$\frac{\kappa_\nu[n_1, U]}{n_1} = \frac{\kappa_\nu[n_2, U]}{n_2},$$

where U is the ionization parameter. This gives

$$\begin{aligned} \kappa_\nu[n(z), J_\nu(z), T, m] &= \kappa_\nu[\Omega_G Y n_c(1+z)^3, J_\nu(0)(1+z)^4, T, m] \\ &= \kappa_\nu[Y n_c, J_\nu(0)\frac{(1+z)}{\Omega_G}, T, m]\Omega_G(1+z)^3. \end{aligned}$$

Here $n_c = 3H_0^2/8\pi G m_p = 11.2\times10^{-6}h_{100}^2\,\mathrm{cm}^{-3}$ is the critical baryon density. The hydrogen density is related to the baryon density by $n_0 = \Omega_G Y n_c$, where $Y = 0.76$ is the fraction of baryons in hydrogen. The above equation shows that the computationally difficult part of the opacity calculation depends only on the two quantities $(1+z)\Omega_G^{-1}$ and T, not on all three variables z, Ω_G, and T. In addition to reducing computation time, use of the homology relation is in fact necessary because CLOUDY is numerically unable to do calculations at the very low densities of the IGM. The actual computations in CLOUDY are all done at a fixed density of $10^{-4}\,\mathrm{cm}^{-3}$.

2.5. Ionization equilibrium

An important assumption which is implicit in our calculation is that ionization equilibrium is established at all epochs. At the very low densities characteristic of the IGM, this assumption requires careful evaluation, in particular for the ionized heavy elements which are responsible for the X-ray opacity. For hydrogen, it is well known that at typical IGM densities and temperatures, the H II recombination time scale can easily be greater than the Hubble time (e.g. Ikeuchi & Ostriker 1986). However, for our purposes this is not a problem because in calculating the ionization state of the heavy elements, we only need to know that the hydrogen is very nearly 100% ionized. Thus the assumption of ionization equilibrium for the heavy elements rests only on their recombination rate coefficients. The two most important processes are radiative recombination and dielectronic recombination. These two rates can be approximated over the temperature range 10^4 - $10^{7.5}$ K by the following formulas (Shull & Van Steenberg 1982):

$$\alpha_{rad}(T) = A_{rad}(T/10^4\,\mathrm{K})^{-\chi_{rad}} \tag{5}$$
$$\alpha_{di}(T) = A_{di}T^{-3/2}\exp(-T_0/T)\,[1 + B_{di}\exp(-T_1/T)]\,. \tag{6}$$

The coefficients A_{rad}, χ_{rad}, A_{di}, B_{di}, T_0, and T_1 for each ionization level of the elements C, N, O, Ne, Mg, Si, S, Ar, Ca, Fe, and Ni have been tabulated by Shull & Van Steenberg, based on theoretical and experimental results.

Using Eqns. 5 and 6 we can calculate the recombination time scale of each element and ionic level at redshift z and compare this to the age of the universe at that epoch. The main result of this calculation is that for the values of temperature and density for which there is significant X-ray optical depth (i.e. the parameter values where we can set constraints on the IGM, as given in Sections 3.2. and 3.3.), the recombination time scale is generally less than the age of the universe. As an example, in Figure 2 we plot lines which indicate the temperature and density at which the two time scales are equal, for the dominant ionization levels of oxygen and iron. In the region to the right of each line, ionization equilibrium is a reasonable approximation. Comparison of oxygen and iron illustrates a general trend that the heavier elements are in equilibrium over a larger region, primarily because the radiative recombination coefficient scales roughly as atomic number squared. It should be noted that at temperatures above $\sim 10^6$ K, the primary contribution to the X-ray optical depth comes from iron, and so the fact that oxygen and other lighter elements are not in equilibrium does not significantly alter our limits on the IGM.

3. High-redshift regime ($z \approx 3$)

3.1. Optical depth

Given the assumptions we have made, we can now calculate the optical depth due to the IGM as a function of six variables, $\tau_\nu = \tau_\nu(\Omega_G, T, m, J_{21}, \Omega_0, z)$. It is informative to show examples of the optical depths, and also illustrate their dependence on the various input parameters. In all cases, unless otherwise specified, we use the following reference values: $z = 3$, $\Omega_0 = 1$, $\Omega_G = 0.1$, $J_{21} = 1.0$, $m = 0.1$, and $T = 10^6\,$K.

The optical depth due to the IGM for the $z = 3$, ($J_{21} = 1.0$, $m = 0.1$, and $\Omega_0 = 1$) is shown in Figure 3. Here we have plotted the optical depth, multiplied by the value indicated in each plot, over grid of values of Ω_G and T. This shows the general dependence of the optical depth on density and temperature.

The dependence of optical depth on J_{21}, the strength of the ionizing background radiation, is shown in Fig. 4. Here we see more than a factor of ten decrease in the optical depth between negligible radiation ($J_{21} = 10^{-3}$) and a realistic radiation strength ($J_{21} = 1$). This shows that any observational limits on IGM properties which do not account for the ionizing radiation must be viewed with caution, in particular the results of SB.

The importance of the ionizating radiation is also evident in Fig. 7, where we show the scaling of the optical depth with IGM density Ω_G. Here we have plotted the quantity τ_ν/Ω_G, which in the absence of a radiation field would be independent of Ω_G. We see, however, that there is a strong dependence, and a factor of 10 decrease in Ω_G results in about a factor of 50 decrease in τ_ν. This is primarily due to the increase in the ionization parameter, although it should be noted that decreasing the density is not simply equivalent to increasing J_{21}, because of density dependent atomic processes such as collisional ionization in the equilibrium calculations.

In Fig. 5 we show the temperature dependence of the optical depth for $T = 10^4$ to $10^8\,$K. The strong decline in τ_ν reflects the trend that at higher temperatures the atoms are more highly ionized, and that the absorption cross-section is lower for higher ionic levels. The peak at 0.1 keV is due to helium and can be seen to become unimportant at $T \gtrsim 10^6\,$K, where almost all of the helium is fully ionized. We also see from Fig. 5 that τ_ν peaks at higher energies as temperature increases, because the K-edge energy increases at higher ionization level. A specific example of the absorption opacity for oxygen ions O V - O VIII is given in Fig. 6, and illustrates dependence of cross-section and K-edge energy on ionization level.

The relative contribution of the important heavy elements in our calculation can be illustrated in two ways. First, in Fig. 8 we plot the optical depth due to each element at the reference IGM parameter values. This shows that oxygen and iron are the most important elements, followed by carbon and neon. The relative strength of these elements is a strong function of temperature, as shown in Fig. 9. Here we plot the peak optical depth due to oxygen and iron as a function of temperature. In oxygen, as the temperature increases above 10^6 K, a significant fraction of the atoms become fully ionized and lose their photoabsorptive opacity. This is not the case for iron, and hence the change in relative optical depth.

3.2. IGM constraints

The X-ray spectra of high redshift quasars are found in many cases to show strong low-energy cut-offs (Elvis et al. 1994). The origin of the cutoffs is not fully understood, although recent work indicates that at least in some cases the absorption is due to warm gas associated with the quasar (Fiore et al. 1993; Mathur et al.1994). This absorption cannot, however, arise in an isotropic IGM because there exist some high-z quasars whose X-ray spectra are well fit by a single power-law with only Galactic absorption. The existence of these quasars implies that with the current data it is only meaningful to set limits on the conditions of the IGM. Currently, we know of three quasars which are at $z > 2$ and have an unabsorbed PSPC spectrum with at least 300 counts: PKS 0237-233 (927 counts), Q0420-388 (363 counts; Elvis et al. 1994), and Q1445+101 (OQ172; 656 counts).

For each quasar spectrum at an observed redshift z the optical depth can, given our assumptions, be calculated as a function of Ω_G, T, m, J_{21}, and Ω_0. In order to compare our results with previous work constraining the nature of the IGM, it is convenient to calculate the optical depth over a grid of values for Ω_G and T, for specified reasonable values of m, J_{21} and Ω_0. For each value of Ω_G and T, we fit the observed quasar PSPC energy spectrum with an absorbed power-law of the form

$$f_\nu^G = C\, W_\nu(N_{\rm H\,I}) \cdot \nu^{-\alpha} \cdot \exp\{-\tau_\nu(\Omega_G, T)\}, \tag{7}$$

where C is a normalization constant and $W_\nu(N_{\rm H\,I})$ is the Wisconsin model of absorption due to Galactic gas (Morrison & McCammon 1983), with the neutral hydrogen column density fixed at the value derived from 21 cm observations. Only the parameters C and α are free to vary. We then calculate the statistic

$$\Delta\chi^2(\Omega_G, T) = \sum_{\rm quasars} \chi^2(\Omega_G, T) - \chi^2(\Omega_G = 0).$$

The function $\Delta\chi^2(\Omega_G, T)$ is distributed as χ^2 with two degrees of freedom, which we use to define confidence intervals in which absorption due to an IGM can be excluded.

In Fig. 10 we illustrate the effect of including the IGM X-ray absorption term in the model fitting of PKS 0237-233, for IGM parameters $T = 10^6$ K, $J_{21} = 1$, $m = 1.0$, and

$\Omega_G = 0.05$ (left side) and $\Omega_G = 0.3$ (right side). In both plots the points are the "intrinsic" X-ray spectral data, in which the PSPC instrument response has been deconvolved, and the solid line is the best fit power-law $\times$ Galactic absorption $\times$ IGM absorption model. For $\Omega_G = 0.05$ the IGM model is consistent with the observed data, whereas for $\Omega_G = 0.3$, the IGM opacity produces a broad absorption trough of width $\Delta E \approx 0.5\,\mathrm{keV}$ and maximum optical depth $\tau \approx 1$. This results in a statistically unacceptable increase in the fit χ^2, and we can rule out an IGM with the given parameters.

In Fig. 11 we plot the 3-σ contour lines of $\Delta\chi^2(\Omega_G, T)$ for the three quasars in our sample for various values of J_{21}, Ω_0, and m. An IGM which is colder or denser than the limits shown is excluded by the observed lack of X-ray absorption. In the left-hand plots we show the results for $J_{21} = 1.0$, which is the most reasonable strength of the ionizing background radiation; in the right-hand plots we use $J_{21} = 0.1$, which is likely the smallest reasonable value. In the upper and lower plots we show the cases $\Omega_0 = 1$ and $\Omega_0 = 0.2$, respectively. In each plot we have drawn contours calculated for an IGM with heavy element abundances of $m = 1, 0.1, 0.01$, and primordial. The vertical dashed line shows for reference the limit on the IGM density imposed by the standard model of big bang nucleosynthesis, $\Omega_B < 0.026 h_{100}^{-2}$, for our adopted value $h_{100} = 0.75$. We also mark the density and temperature of the diffuse IGM predicted by CO93.

3.3. Discussion

Comparison of the left and right sides of Fig. 11 shows the strong dependence of the X-ray constraints on the assumed ionizing background. This is important to note because previous work which predicted strong constraints (SB, Rees & Sciama 1967) did not take this background into account. The effect of this radiation is to ionize more highly the heavy elements which contribute to the X-ray opacity, thereby reducing the overall absorption cross-section.

Inspection of Fig. 11 shows that for a primordial IGM, the X-ray Gunn-Peterson test we have calculated is not particularly sensitive. Referring back to Fig. 8 we see that the absorption due to helium is relatively weak and more importantly it is confined to energies $h\nu \lesssim 0.3\,\mathrm{keV}$. Since Galactic absorption is significant at this energy, the quasar spectra have much lower signal to noise in this region. It should be noted here that the He II($\lambda 304$Å) line is expected to have a very large optical depth for reasonable IGM models. For instance, CO93 predict that at $z = 3$ the optical depth is approximately 1000. This line has not been observed because in all currently known QSOs with $z > 3$ (which corresponds to rest-frame 304 Å for an observed-frame wavelength of 1215 Å), there is an intervening Lyman-limit system which blackens the spectrum in the relevant wavelength range. Some recent HST observations have come frustratingly close, for instance the $z = 2.72$ which has no optically thick Lyman-limit systems (Reimers et al.1992). It is somewhat ironic to note that if the optical depth is as large as predicted, it will be difficult to usefully constrain the IGM properties, apart from proving the existence of the IGM.

For an enriched IGM the X-ray Gunn-Peterson test is much more sensitive than for a primordial IGM, since as we have seen in Sec. 3.1., most of the X-ray opacity is due to heavy elements such as oxygen, iron, neon, and carbon. We can now examine Fig. 11 to determine the lower bounds on IGM temperature for various values of J_{21} and abundance, at two interesting IGM densities, $\Omega_G = 0.06$ and $\Omega_G = 1.0$. In the former case the IGM makes up the bulk of the baryonic matter predicted by standard big bang nucleosynthesis, while in the latter case the IGM contains the baryonic matter necessary to close the universe. With $\Omega_G = 1.0$, a non-standard model for nucleosynthesis must be adopted in order not to conflict with the observed light element abundances. Despite the success of the standard model, one should not dismiss entirely the alternatives (e.g. Dimopoulos et al. 1988; Turner 1988). From the figure we see that if the ionizing background radiation is as strong as $J_{21} = 1.0$, then our X-ray Gunn-Peterson test does not constrain the temperature (above 10^4 K) of an IGM with $\Omega_G = 0.06$, even with solar abundances. For an IGM with the closure density, we see from Fig. 11 that we can significantly constrain the temperature, especially for the weak ionizing background case. However, it should be noted that in this case, with such a large amount of matter in the IGM, it is unlikely that any enrichment processes are efficient enough to produce a heavy element abundance above 0.01 solar. In all cases, comparison with the IGM temperature and density predicted by CO93 as shown in Fig. 11 reveals that the X-ray opacity of a hot diffuse IGM is too small to test their prediction with the current data.

In order to investigate the ultimate utility of the X-ray Gunn-Peterson test using PSPC spectra, we have constructed simulated PSPC spectra with higher signal to noise and carried out the procedure described in Sec. 3.2. The simulated data were created using the best fit power-law with Galactic absorption model for PKS0237-233, with roughly 10,000 and 100,000 counts, respectively. We find that the factor of 100 in counts gives only a factor of 5 improvement in the density limit at constant temperature, for $J_{21} = 1.0$ and $m = 0.1$. On the other hand, at a given density the temperature limit scales almost linearly with number of counts. For solar abundance with $J_{21} = 1.0$, or 0.1 solar with $J_{21} = 0.1$, a quasar with 10^5 counts and no observed absorption would exclude a large range of temperatures and densities. However, even in these cases, the test would not be sensitive enough to test the predicted IGM properties from CO93.

4. Low-redshift regime ($z \lesssim 0.4$)

The calculations of SB showed that the IGM optical depth at low redshift ($z \lesssim 0.4$) has a qualitatively different character than at high redshift. In the low-redshift case the optical depth is dominated by narrow absorption "troughs", with sharp edges and fractional width $\Delta E/E \approx z$. The peak optical depth due to the IGM is much smaller than at high redshift. However, it is possible to take advantage of the very distinctive absorption troughs, as well as the much higher signal-to-noise possible in nearby low-redshift quasars, to compensate for the weakness of the absorption. We now consider the question of detecting or constraining the IGM using low-redshift quasars.

4.1. Optical depth

The optical depth due to the IGM for the low-redshift case $z = 0.15$ ($J_{21} = 1.0$, $m = 0.1$, and $\Omega_0 = 1$) is shown in Figure 12. Here we have plotted the optical depth, multiplied by the value indicated in each plot, over grid of values of Ω_G and T. The strong peaks and discontinuities in the optical depth reflect that, in contrast to the high-redshift case, the dominant contributor here is the opacity from atomic line transitions. From Equation 3 we see that the absorption due to a line with rest frequency ν_α is "redshifted" over the frequency range $\nu_\alpha(1+z)^{-1} \le \nu \le \nu_\alpha$. At the edges of this range the optical depth due to the line drops discontinuously to zero. The discrete nature and well-defined wavelengths of the absorption troughs allow for easy identification of the species responsible for the opacity. For instance, for $\Omega_G = 1.0$ and $T = 10^6$ K, the dominant lines are C V, C VI, N VI, N VII, O VII, O VIII, Fe XIX, and Fe XX. The largest peak, starting at 0.5 keV, is a blend of O VII and O VIII. These two lines show the temperature dependence of the ionization equilibrium, most clearly at low densities. At $\Omega_G = 0.1$ and $T = 10^4$ K, O VII predominates, while at $T = 10^6$ K the dominant ion is O VIII. Figure 12 also shows that at high density and low temperature there is significant continuum opacity due to helium.

4.2. IGM detection limits

We first consider detection of absorption due to the IGM using existing X-ray satellite data. The ROSAT PSPC has energy resolution $E/\Delta E \sim 4$, which is too low even to resolve the absorption trough and is hence unsuitable this type of invesigation. The ASCA SIS instrument has sufficient resolution, $E/\Delta E \sim 15$ at 1 keV, to begin resolving the trough for

$z \gtrsim 0.15$, but it is inadequate to determine the trough shape. For both these instruments, if a quasar is found which is well-fitted by a power-law and Galactic absorption model, then the same technique we described for high-redshift quasars can be applied to constrain the IGM properties. However, at very high signal-to-noise one begins to see intrinsic deviations from a power-law, possibly due to intervening cold or warm material in the line of sight to the X-ray source (Elvis et al. 1994; Mathur et al. 1994) or Compton reflection from an accretion disk (White, Lightman, & Zdziarski 1988; Lightman & White 1988). In addition, it is difficult to calibrate the energy response in X-ray mirrors and spectrometers to much better than a few percent, and in particular it is difficult to determine the exact depth of absorption edges due to material in the mirrors and other components. These two effects generally produce X-ray spectra that have structure beyond a simple power-law, considerably weakening any conclusions about a possible IGM based on low to moderate resolution spectra. It is interesting to note that the power-law fit to one of the ROSAT PSPC spectra of 3C 273 (obtained from the ROSAT archive) is substantially improved by the addition of IGM absorption with $\Omega_G = 1.0, T = 10^{5.3}$ K, $m = 0.1$, and $J_{21} = 1.0$. In this case the fit statistic changes from $\chi^2 = 70$ (25 DOF) to $\chi^2 = 39$ (23 DOF), which has an F-test probability of much less than 1%. However, such a cool, dense IGM is ruled out by the Ly-α Gunn-Peterson test, hence illustrating the problems inherent in using low-resolution, high signal-to-noise spectra to derive IGM properties.

However, if the spectral resolution is high enough ($E/\Delta E \gtrsim 100$ at 1 keV) then the absorption troughs can be used to identify or constrain IGM absorption with much greater confidence. Instead of focusing on the overall fit of a spectral model (power-law $\times$ Galactic absorption $\times$ IGM absorption) as in the high-redshift case, we determine a local continuum near the known position of strong lines. We then sum the spectrum over the extent of the absorption trough for a particular line, which then allows calculation of the trough optical depth. The two problems mentioned previously, uncertainty in both the quasar spectrum and detector energy calibration, can be avoided by carefully selecting energy bands (for the continuum and absorption trough) which are free of any contaminating sharp edges or lines.

Since it is evident from Fig. 12 that O VII (0.574 keV) and O VIII (0.654 keV) are the strongest lines over most of the range where the IGM has significant optical depth, we now look in detail at possible detection of these two lines. In Fig. 13 we show a schematic diagram of a quasar spectrum at $z = 0.15$ which shows absorption due to N VI, O VII, and O VIII in the IGM, along with the edges and lines which can be potential sources of uncertainty in the spectrum. In this energy range, the important spectral features intrinsic to the quasar are possible absorption lines due to a warm absorber containing O VII or O VIII. Most evidence indicates that these absorbers are associated with the quasar, and are due to either a previously unidentified component which also gives rise to UV absorption

(Mathur et al. 1994; Mathur 1994) or broad emission line clouds (Shields, Ferland, & Peterson 1994). In both cases the velocity of the material with respect to the quasar will be less than about 5000 km s^{-1}, and hence the regions further than about 9 eV from the line energy will be unaffected. Note that these lines will be redshifted because they are associated with the quasar. The only strong spectral feature expected in the mirror and spectrometer energy response in this energy range is the O I K-edge (0.532 keV).

If we now make the conservative presumption that the strengths of the warm absorber lines and energy response edges are not well known, the energy ranges which can be used to search for IGM absorption are limited. Any region which contains a possible intrinsic line or crosses an edge boundary is excluded. It is particularly important to insure that there be no edge between the regions used to determine the continuum and the IGM absorption. The regions which are free of contamination and can be used for determining the O VII and O VIII absorption trough optical depth are drawn in bold in Figure 13. From our discussion and Figure 13 it is apparent that in most cases the continuum can be determined only on one side of the absorption trough. In this case the local spectral slope is determined by the spectral model. In practice, this means using the fit residuals instead of the raw spectrum for calculating the continuum and trough counts.

As a specific example of the previous discussion, we now consider the AXAF low-energy transmission grating spectrometer (LETGS), which will have an energy resolution of roughly 500 near 0.5 keV. This is sufficient to allow discrimination of the contaminating edges and lines. For a specified source flux and observation time, we can calculate the expected number of counts in the clean energy bands and thus determine the absorption trough optical depth which could be detected. We then compare this limit to the predicted optical depth of the troughs for given IGM parameters ($\Omega_G, T, m, J_{21}, \Omega_0$) and so determine the ranges over which the IGM could be constrained or detected. To estimate the expected number of counts, we assume a spectrum which is a power-law with energy index -0.7 and with absorption due to a Galactic neutral hydrogen column density $N_H = 2\times10^{20}\,\mathrm{cm}^{-2}$. The $3\,\sigma$ optical depth detection limit for this spectral shape, based on counting statistics and using $\tau \ll 1$, is

$$\tau < 0.1\left(\frac{1+\Delta E_c/\Delta E_a}{2}\right)^{1/2}\left(\frac{E}{0.5\,\mathrm{keV}}\right)^{0.7}\left[C_p\left(\frac{\Delta E_c}{0.1\,\mathrm{keV}}\right)\left(\frac{A(E)}{20\,\mathrm{cm}^2}\right)\left(\frac{t}{10^5\,\mathrm{s}}\right)\right]^{-1/2}. \tag{8}$$

Here ΔE_c and ΔE_a are energy widths over which the continuum and absorption trough counts are summed, respectively, E is the central energy of the trough, C_p is the ROSAT PSPC unfiltered count rate, $A(E)$ is the effective area of the X-ray spectrometer, and t is the duration of the observation. For reference, $C_p = 1$ corresponds to an energy flux $F = 1.1\times10^{-11}\,\mathrm{erg\,s^{-1}\,cm^{-2}}$ (0.1 - 2.4 keV) or $F = 1.5\times10^{-11}\,\mathrm{erg\,s^{-1}\,cm^{-2}}$ (2 - 10 keV).

In the left-hand plot of Figure 14 we show the 3σ detection limits for O VII and O VIII from Eqn. 8 for a spectrum equivalent to a 100 ksec observation of 3C 273 by the AXAF LETGS. This assumes an effective area $A(E) = 20\,\mathrm{cm}^2$ and a PSPC count rate of $C_p = 6\,\mathrm{cts\,s}^{-1}$, for $z = 0.15$. We use energy bands for the continuum and trough shown in Figure 13, which gives a 3σ detection limit of $\tau \approx 0.1$. In both of the plots, the solid line and dashed line correspond to $J_{21} = 1.0$ and $J_{21} = 0.1$, respectively. The bold lines are for heavy element abundance $m = 1.0$ and the medium lines are for $m = 0.1$. For $m = 0.01$, the IGM optical depth is too low to detect the IGM in the range we have plotted. We also show for reference the big-bang nucleosynthesis limit (BBN), the Ly-α Gunn-Peterson limit, and the IGM temperature and density predicted by CO93. The plot illustrates that in some cases the sensitivity increases at higher temperature, for a given density. This simply a reflection of the temperature and density regime in which O VII and O VIII are the dominant oxygen species in the ionization equilibrium. The overall result shown in the plots is that only in the cases of nearly solar heavy element abundance ($m = 1.0$) or high density ($\Omega_G \approx 1$) will the X-ray spectra of low-redshift quasars be sensitive to absorption caused by the IGM. In no cases can the test detect an IGM at the temperature and density predicted by CO93.

Looking optimistically to future X-ray telescopes, we show in right-hand plot of Figure 14 the 3σ detection limits for a telescope effective area of $2000\,\mathrm{cm}^2$, which is a factor of 100 increase over the AXAF LETGS. With this effective area the detection limit is $\tau \approx 0.01$, below which it will be very difficult indeed to make any convincing determination that an absorption trough is present. This plot shows that with such a large effective area the X-ray Gunn-Peterson test is sensitive to an IGM with $m = 1.0$ and temperature and density near that predicted by CO93. For $m = 0.1$, the test can detect the IGM for temperature $T \lesssim 10^6\,\mathrm{K}$ for $J_{21} = 0.1$. For $m = 0.01$ the test is unable to detect the IGM outside the current Ly-α Gunn-Peterson limits.

Although we have shown only the IGM detection limits for the case $z = 0.15$, we have also calculated these limits for several other redshifts and we find that they are largely insensitive to z in the range $0.15 \lesssim z \lesssim 0.25$. Outside this range, the widths of the regions over which the continuum or the trough counts are summed become small, with a corresponding decrease in sensitivity.

5. Summary

We have derived the constraints which can be placed on the density and temperature of the IGM based on ROSAT PSPC X-ray spectra of $z \approx 3$ quasars, as well as the expected detection limits based on high-resolution ($E/\Delta E \gtrsim 100$) spectra of $z \lesssim 0.4$ quasars. In order to calculate the X-ray optical depth due to the IGM, we made the following assumptions: the IGM is isotropic with no redshift evolution of density Ω_G and temperature; the heavy-element abundances are independent of redshift and are uniformly depleted from the "cosmic" abundances of Cameron (1973); the UV to soft X-ray background radiation spectrum scales with redshift as $(1+z)^4$; and ionization equilibrium can be assumed to hold for the heavy elements. Given these assumptions, we have shown how to calculate the optical depth due to the IGM as a function of redshift (z), total mass density (Ω_0), IGM density (Ω_G), temperature (T), heavy element abundance (m), and background radiation strength (J_{21}). The calculation of ionization equilibrium is done entirely within the program CLOUDY.

We find the following about our model of the X-ray optical depth of the IGM out to high redshift. The ionizing background radiation, which was not included in previous calculations of this nature, strongly affects the optical depth. Changing the background strength from $J_{21} = 10^{-3}$ to $J_{21} = 1$ decreases the peak optical depth by over a factor of 10. In addition, the background radiation causes the optical depth to be non-linear in Ω_G, and for $J_{21} = 1$, a factor of 10 decrease in Ω_G results in a factor of over 50 decrease in optical depth. Our calculations reveal that at high redshift the X-ray optical depth is dominated by the heavy element edge transitions O-K, Fe-L, Ne-K, and C-K. Below about 10^6 K, oxygen is the most important, while for higher temperatures iron is the largest contributor.

The constraints on IGM temperature and density were made by choosing representative values for the parameters Ω_0, m, and J_{21} and calculating the optical depth for each quasar redshift z over an array of values of Ω_G and T. This optical depth was incorporated into the X-ray spectral fitting model for that quasar, and we determined the IGM parameter values for which the model produced an unacceptable fit. The was done for the three $z \approx 3$ quasars PKS 0237-233, Q0420-388, and OQ172.

We find that if the IGM density is at the limit allowed by the standard theory of big bang nucleosynthesis ($\Omega_G \leq 0.026h_{100}^2$), the X-ray Gunn-Peterson test with high-redshift ROSAT PSPC spectra can significantly constrain the temperature of the IGM only for nearly solar heavy element abundances ($m \approx 1$). For a temperature of 10^5 K and $m = 0.1$, this test limits the density to $\Omega_G \lesssim 0.3$. Near the IGM density and temperature predicted by CO93, the X-ray optical depth is negligible ($\tau_\nu < 0.01$). Simulated PSPC spectra with up to 100,000 counts were created and we found that even with such high signal to noise, the test would not be sensitive to the predicted IGM. We conclude that with the energy resolution available in ROSAT data, the X-ray optical depth out to high redshift allows substantial constraint of the IGM only in the cases of nearly solar heavy element abundance or density near that required to close the universe.

For low-redshift quasars ($z \lesssim 0.4$) the IGM X-ray optical depth is generally less than unity and is dominated by sharp absorption troughs. Constraining or detecting the IGM in this regime therefore requires high signal-to-noise, at which point intrinsic deviations from a power-law spectrum are usually apparent. We have presented a detection method which minimizes the effect of these uncertainties by avoiding contaminating edges and lines in the spectrum. Using this method and two assumed values of the X-ray spectrometer effective area ($20\,\mathrm{cm}^2$, equivalent to the AXAF LETGS, and $2000\,\mathrm{cm}^2$) we have derived the temperature and density ranges over which the IGM could be detected. At plausible densities, the IGM out to $z = 0.15$ could not be detected with an AXAF LETGS spectrum equivalent to a 100 ksec observation of 3C 273. However, with the large area detector, the IGM could be detected over a substantial range of temperatures and densities.

Acknowledgments

The authors wish to thank Belinda Wilkes for supplying the PSPC spectrum of PKS 0237-233 in advance of publication, Gary Ferland for help with CLOUDY, Adam Dobrzycki and Smita Mathur for useful discussions, and Claude Canizares for initially suggesting we do this investigation. The work was supported by NASA grants NAGW-2201 (LTSARP) and NAG 5-1872 (ROSAT).

REFERENCES

Bajtlik, S., Duncan, R. C., Ostriker, J. P., 1988, ApJ, 327, 570

Bechtold, J., 1994, ApJS, in press

Bechtold, J., Weymann, R. J., Lin, Z., & Malkan, M. 1987, ApJ, 315, 180

Cameron, A. G. W. 1973, Space Sci. Rev., 15, 121

Cen, R. & Ostriker, J. P. 1993, ApJ, 417, 404 (CO93)

Dimopoulos, S., Esmailzadeh, R., Hall, L. J., & Starkman, G. D. 1988, ApJ, 330 545

Elvis, M., Fiore, F., Wilkes, B., McDowell, J., & Bechtold, J. 1994, ApJ, in press.

Fall, S. M. & Pei, Y. C. 1993, ApJ, 402, 479

Ferland, G. J. 1993, University of Kentucky Department of Physics and Astronomy Internal Report.

Field, G. B. & Perrenod, S. C. 1977, ApJ, 215, 717

Fiore, F., Elvis, M., Mathur, S., Wilkes, B. J., & McDowell, J. C. 1993, ApJ, 415, 129

Giallongo, E., Cristiani, S., & Trevese, D. 1992, ApJ, 398, L9

Gunn, J. E., & Peterson, B. A. 1965, ApJ, 142, 1633

Hasinger, G., Schmidt, M., and Trümper, J. 1991, A&A, 246, L2

Ikeuchi, S. & Ostriker, J. P. 1986, ApJ, 301, 522

Ikeuchi, S. & Turner, E. L. 1991, ApJ, 381, L1

Kato, T. 1976, ApJS, 30, 397

Kolb, E. W. & Turner, M. S. 1990, The Early Universe, (New York: Addison-Wesley Co.)

Lightman, A. P. & White, T. R. 1988, ApJ, 335, 57.

Mather, J. C., et al. 1993, COBE preprint no. 93-01

Mathur, S., 1994, ApJ, submitted.

Mathur, S., Wilkes, B., & Elvis, M. 1994, ApJ, in press.

Miralda-Escoudé, J. & Rees, M. J. 1994, MNRAS, 266, 343

Morrison, R. & McCammon, D. A. 1983, ApJ, 270, 119

Murdoch, H. S., Hunstead, R. W., Pettini, M., & Blades, J. C. 1986, ApJ, 309, 19

Pfefferman, E., et al. 1987, Proc. SPIE, 733, 519

Rees, M. J. & Sciama, D. W. 1967, ApJ, 147, 353

Reimers, D., Vogel, S., Hagen, H.-J., Engels, D., Groote, D., Wamsteker, W., Clavel, J., & Rosa, M. P. 1992, Nature, 360, 561.

Sarazin, C. L. 1988, X-ray Emission from Clusters of Galaxies, (Cambridge: Cambridge Univ. Press)

Sargent, W. L. W. 1988, in QSO Absorption Lines, eds. J. C. Blades, D. A. Turnshek, and C. A. Norman (Cambridge: Cambridge Univ. Press), p. 1

Shull, J. M. & Van Steenberg, M. 1982, ApJ, 48, 95

Shapiro, P. R. 1989, in Fourteenth Symposium on Relativistic Astrophysics, ed. E. J. Fenyves (Ann. N. Y. Acad. Sci: 571), p. 128

Shapiro, P. R. & Bahcall, J. N. 1980, ApJ, 241, 1 (SB)

Shapiro, P. R., Giroux, M. L., & Bubul, A. 1994 ApJ, in press.

Sherman, R. D. 1979, ApJ, 232, 1

Sherman, R. D. & Silk, J. 1979, ApJ, 234, L9

Shields, J. C., Ferland, G. J., & Peterson, B. M. 1994, ApJ, submitted.

Stanek, K. Z. 1992, MNRAS, 259, 247

Trümper, J. 1983, Adv. Space Res., 2, No.4 241

Turner, M. S. 1988, Phys. Rev. D, 37, 304

White, T. R., Lightman, Ap. P., & Zdziarski, A. A. 1988, ApJ, 331, 939.

Wu, X., Hamilton, T., Helfant, D. J., & Wang, Q. 1991, ApJ, 379, 564

This manuscript was prepared with the AAS LaTeX macros v3.0.

Fig. 1 – Current observational limits on the density and temperature of the IGM. The BBN line is the upper limit for baryonic mass based on standard big bang nucleosynthesis and $H_0 = 75$ km s^{-1} Mpc^{-1}. The temperature and density of the IGM calculated by CO93 and Field & Perrenod (1977; FP77) are marked.

Fig. 2 – Comparison of the recombination time scale for oxygen (left) and iron (right) to the age of the universe at $z = 1$, for the dominant ionization levels in our modeling. The lines indicate the temperature and density at which the recombination time scale is equal to the age of the universe. In the region to the right of each line the species is in ionization equilibrium. On the left side are plotted lines for O IV (solid), O V (dotted), O VI (short dashed), O VII (long dashed), and O VIII (dot-dashed). On the right side are plotted lines for Fe XVII (solid), Fe XVIII (dotted), Fe XIX (short dashed), Fe XX (long dashed), Fe XXI (dot - short dashed), and Fe XXII (dot - long dashed).

Fig. 3 – Optical depth for an array of Ω_G and T, for $z = 3, J_{21} = 1.0, m = 0.1$, and $\Omega_0 = 1$. Each of the sub-plots uses the same axis scalings as in the one marked on the lower lefthand corner. The optical depth in each sub-plot has been multiplied by the value indicated.

Fig. 4 – X-ray optical depth for values of the ionizing background normalization, $J_{21} = 10^{-3}$ (solid), 10^{-2} (dotted), 10^{-1} (short dashed), and 1 (long dashed). All curves are for $z = 3$, $\Omega_0 = 1$, $\Omega_G = 0.1$, $T = 10^6$ K, and $m = 0.1$.

Fig. 5 – Log of the X-ray optical depth for values of the IGM temperature $T = 10^4$ K (solid), 10^5 K (dotted), 10^6 K (short dashed), 10^7 K (long dashed), and 10^8 K (dot dashed). All curves are for $z = 3$, $\Omega_0 = 1$, $\Omega_G = 0.1$, $J_{21} = 1$, and $m = 0.1$.

Fig. 6 – Relative opacity for oxygen ions O V (solid), O VI (dotted), O VII (short dashed), and O VIII (long dashed).

Fig. 7 – Scaling of optical depth with IGM density. We have plotted (τ_ν/Ω_G), which would be independent of Ω_G if there were no background radiation field. In this case, with $J_{21} = 1$, a decrease by a factor of 10 in density results in a decrease in τ_ν of more than a factor of 50. All curves are for $z = 3$, $\Omega_0 = 1$, $J_{21} = 1$, $T = 10^6$ K, and $m = 0.1$.

Fig. 8 – Contribution of individual elements to X-ray optical depth for $z = 3$, $\Omega_0 = 1$, $\Omega_G = 0.1$, $J_{21} = 1$, $T = 10^6$ K, and $m = 0.1$. At this temperature the optical depth is dominated by oxygen and iron.

Fig. 9 – Maximum optical depth due to oxygen (crosses) and iron (circles) as a function of temperature.

Fig. 10 – Illustration of the effect of the IGM X-ray absorption term for $T = 10^6$ K,

$J_{21} = 1$, $m = 1.0$, and $\Omega_G = 0.05$ (left) and $\Omega_G = 0.3$ (right) in the model fitting of PKS 0237-233. The points are the intrinsic X-ray spectrum with the PSPC instrument response deconvolved and the solid lines are the model fits. Clearly $\Omega_G = 0.05$ is consistent with the data while $\Omega_G = 0.3$ is not consistent.

Fig. 11 – 3-σ limits on temperature and density of IGM based on X-ray optical depth toward high-redshift quasars. The regions to the right of and below the lines are excluded. The upper plots show limits for $\Omega_0 = 1$ and the lower plots are for $\Omega_0 = 0.2$. The left plots show limits for background ionizing radiation with strength $J_{21} = 1.0$ and the right plots show limits for $J_{21} = 0.1$. In all plots there are four solid contour lines, which from boldest to thinnest correspond to heavy element abundances $m = 1$, 0.1, 0.01, and primordial ($m = 0$). In the lower two plots, the contour lines are dashed for the unphysical region $\Omega_G > \Omega_0$. We also show the limits due to big bang nucleosynthesis (BBN) and Ly-α Gunn-Peterson, as well as the IGM temperature and density predicted by CO93.

Fig. 12 – Optical depth for an array of Ω_G and T, for $z = 0.15, J_{21} = 1.0, m = 0.1$, and $\Omega_0 = 1$. Each of the sub-plots uses the same axis scalings as in the one marked on the lower lefthand corner. The optical depth in each sub-plot has been multiplied by the value indicated.

Fig. 13 – Schematic diagram of quasar power-law continuum, with O VII and O VIII IGM absorption, as well as with potential sources of uncertainty in spectrum arising from intrinsic absorption in quasar and imperfect knowledge of detector energy response. The spectral ranges drawn in bold are used for summing the continuum and absorption trough counts.

Fig. 14 – 3σ detection limits for a spectrum equivalent to a 100 ksec observation of 3C 273 ($z = 0.15$) by a detector with effective area $A = 20\,\mathrm{cm}^2$ (AXAF LETGS) and $A = 2000\,\mathrm{cm}^2$. The solid and dashed lines correspond to $J_{21} = 1.0$ and $J_{21} = 0.1$, respectively. The thick, medium, and thin lines are for heavy element abundances $m = 1.0, 0.1$, and 0.01, respectively. Also shown for reference are the big-bang nucleosynthesis limit (BBN), the Ly-α Gunn-Peterson limit, and the IGM temperature and density predicted by CO93.

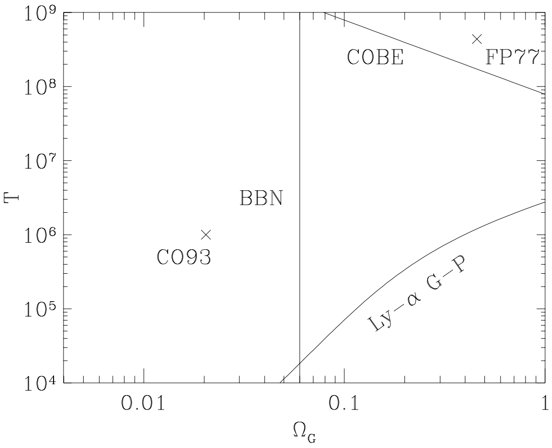
COBE
FP77
BBN
CO93
Ly–α G–P
T
Ω_G
10^9
10^8
10^7
10^6
10^5
10^4
0.01
0.1
1

Fig. 1.—

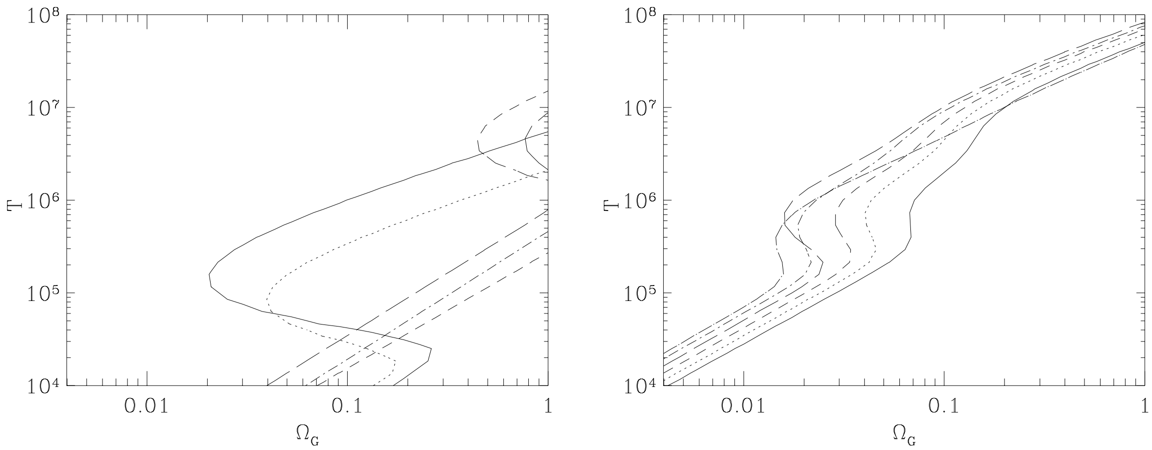
T
Ω_G
10^8
10^7
10^6
10^5
10^4
0.01
0.1
1

Fig. 2.—

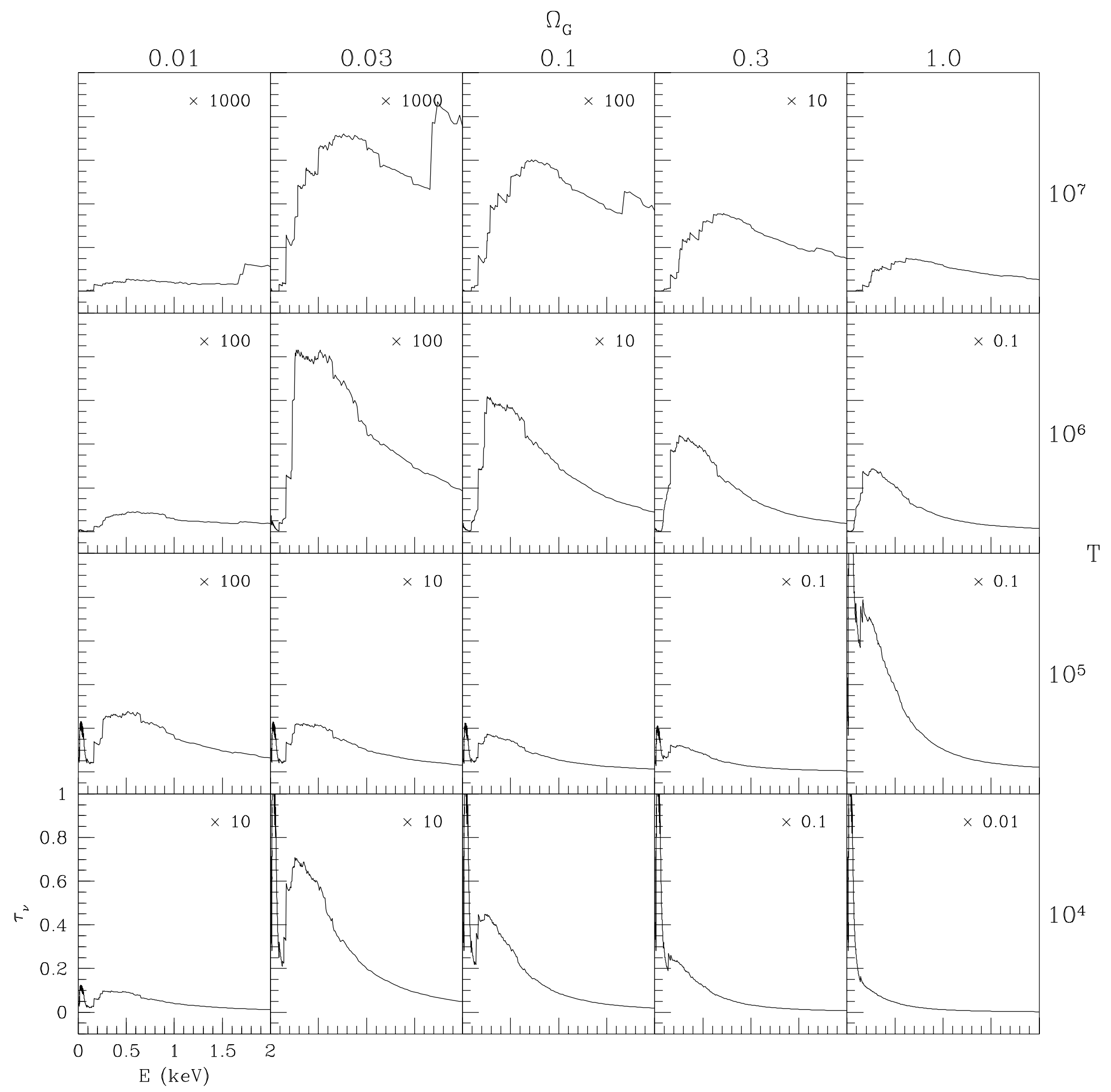
Ω_G
0.01
0.03
0.1
0.3
1.0
T
10^7
10^6
10^5
10^4
× 1000
× 1000
× 100
× 10
× 100
× 100
× 10
× 0.1
× 100
× 10
× 0.1
× 0.1
× 10
× 10
× 0.1
× 0.01
τ_ν
E (keV)

Fig. 3.—

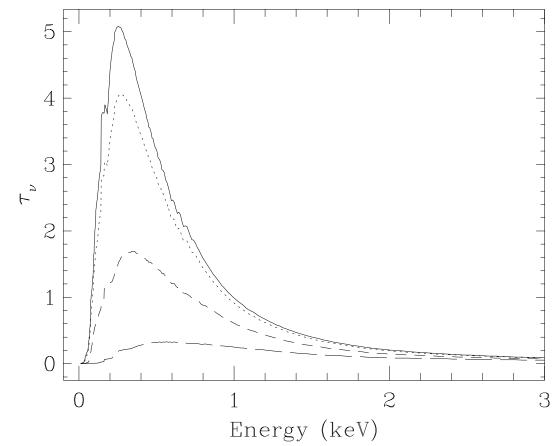

Fig. 4.—

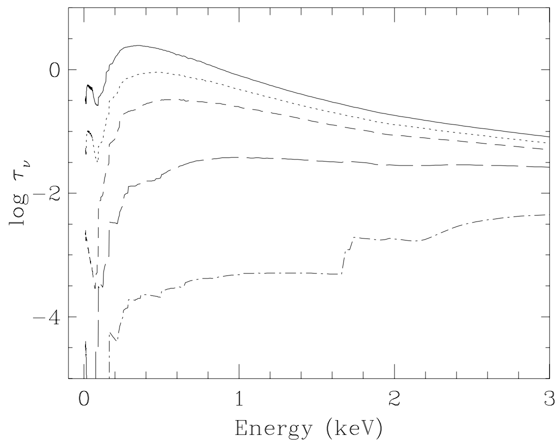

Fig. 5.—

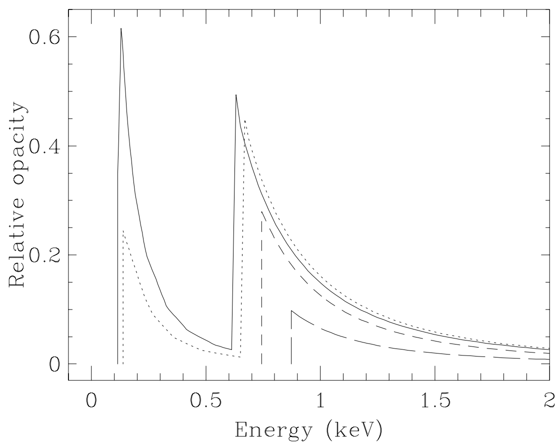
Relative opacity
0.6
0.4
0.2
0
0
0.5
1
1.5
2
Energy (keV)

Fig. 6.—

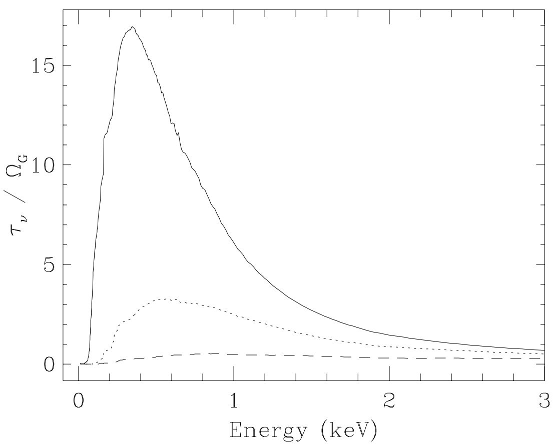
τ_ν / Ω_G
15
10
5
0
0
1
2
3
Energy (keV)

Fig. 7.—

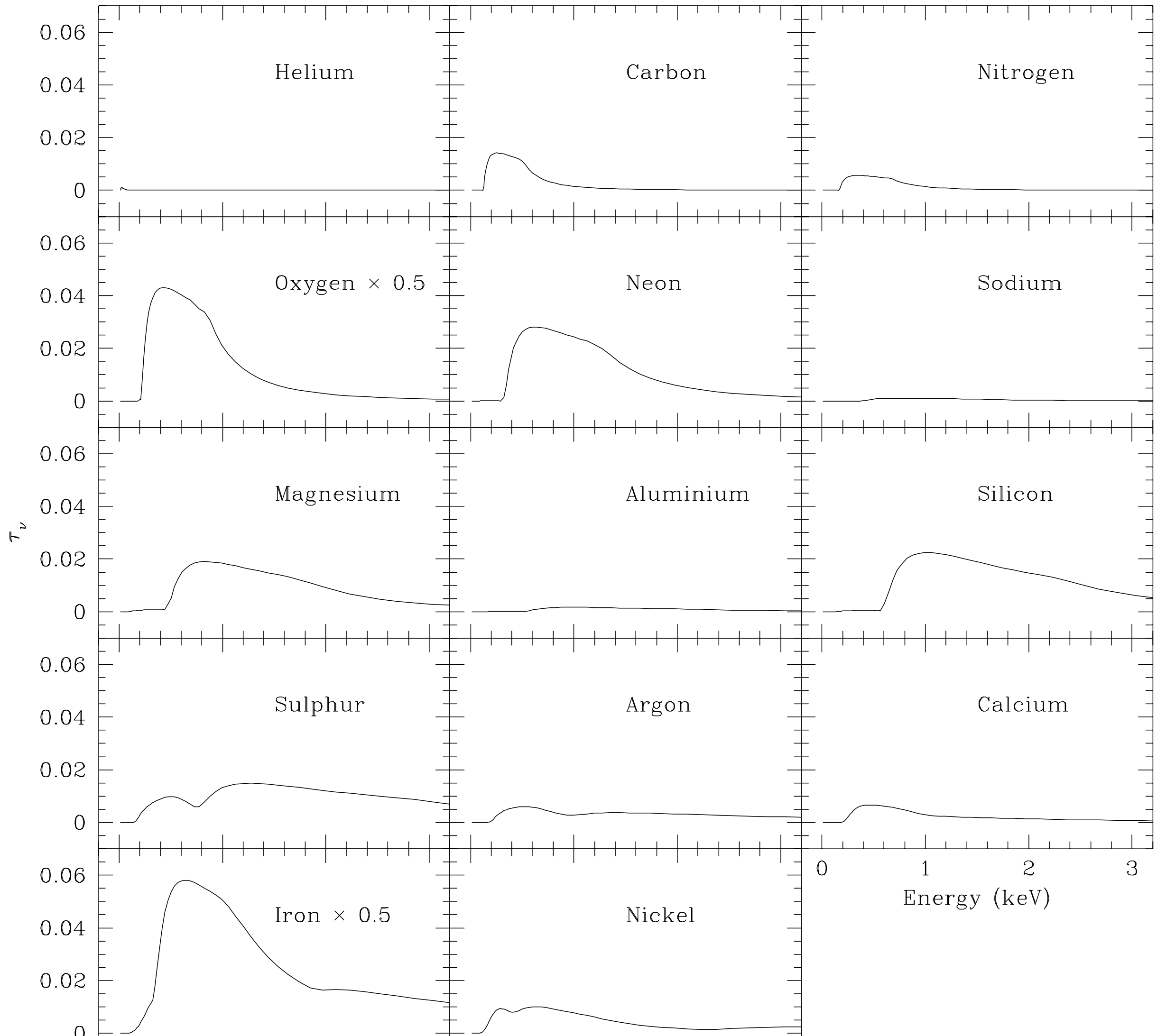
Helium
Carbon
Nitrogen
Oxygen × 0.5
Neon
Sodium
Magnesium
Aluminium
Silicon
Sulphur
Argon
Calcium
Iron × 0.5
Nickel
τ_ν
0.06
0.04
0.02
0
0
1
2
3
Energy (keV)

Fig. 8.—

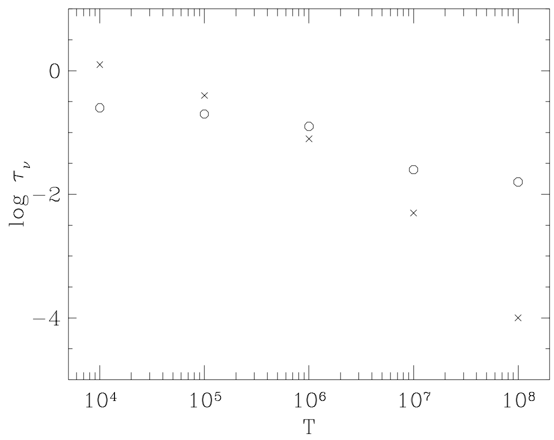
log τ_ν
T
0
−2
−4
10^4
10^5
10^6
10^7
10^8

Fig. 9.—

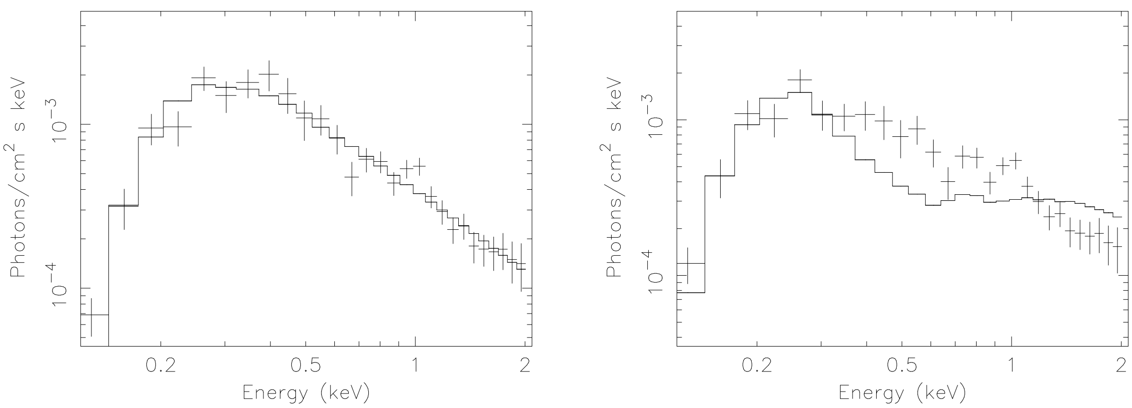
Photons/cm^2 s keV
10^{-3}
10^{-4}
0.2
0.5
1
2
Energy (keV)

Fig. 10.—

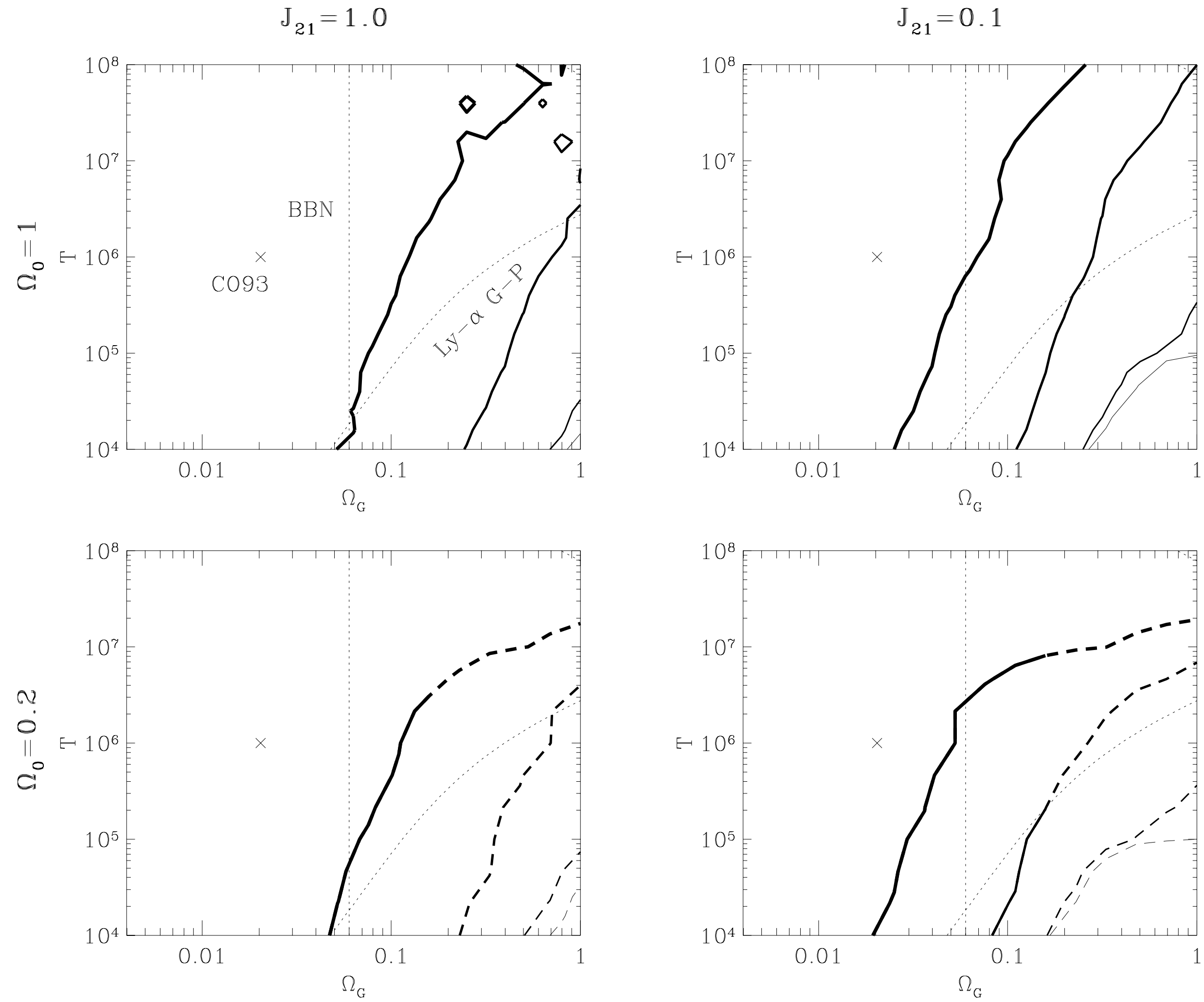

J21=1.0
J21=0.1
Ω0=1
Ω0=0.2
T
ΩG
BBN
CO93
Ly–α G–P
10^4
10^5
10^6
10^7
10^8
0.01
0.1
1

Fig. 11.—

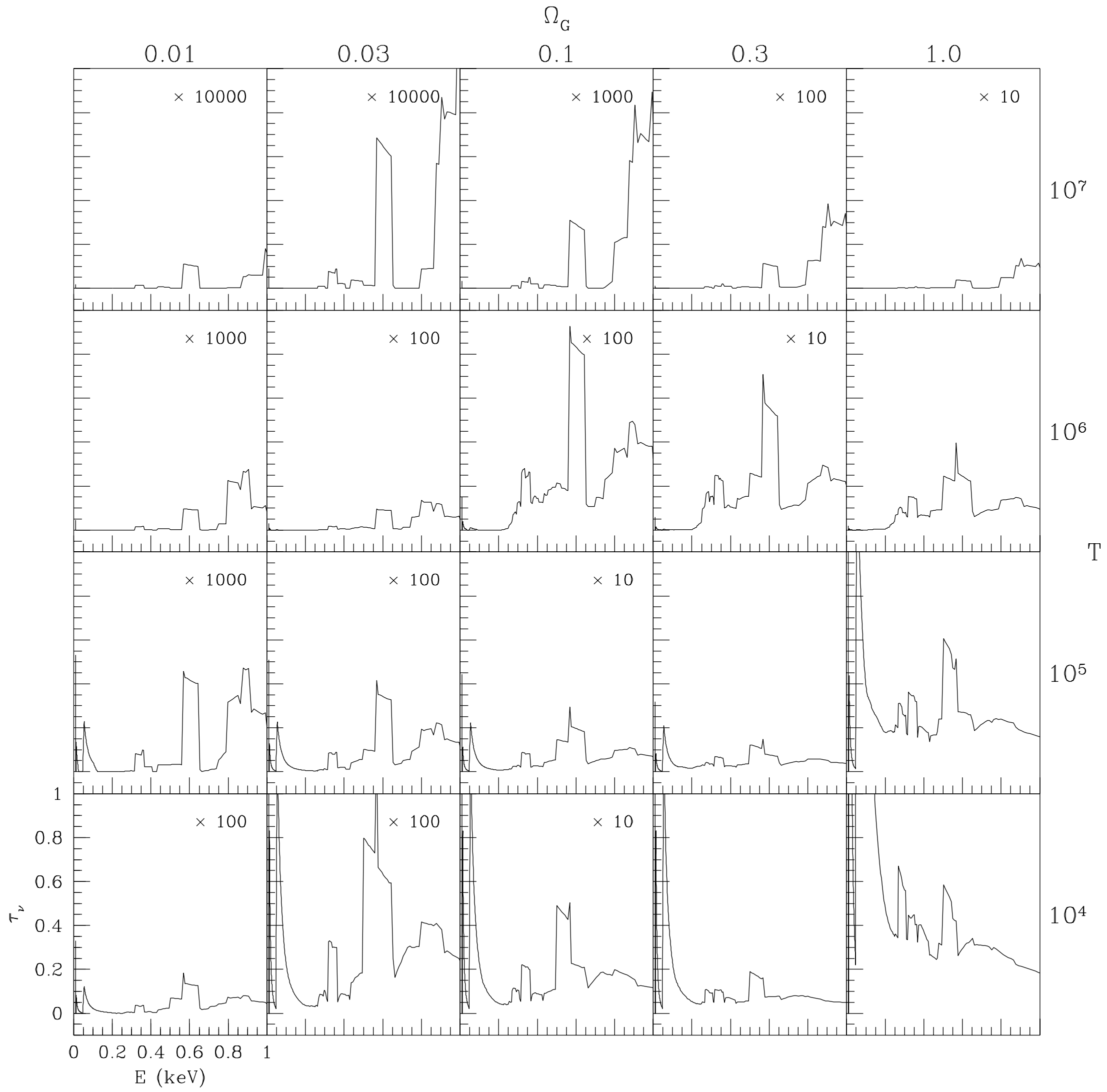
Ω_G
0.01
0.03
0.1
0.3
1.0
× 10000
× 10000
× 1000
× 100
× 10
10^7
× 1000
× 100
× 100
× 10
10^6
T
× 1000
× 100
× 10
10^5
× 100
× 100
× 10
10^4
τ_ν
1
0.8
0.6
0.4
0.2
0
0 0.2 0.4 0.6 0.8 1
E (keV)

Fig. 12.—

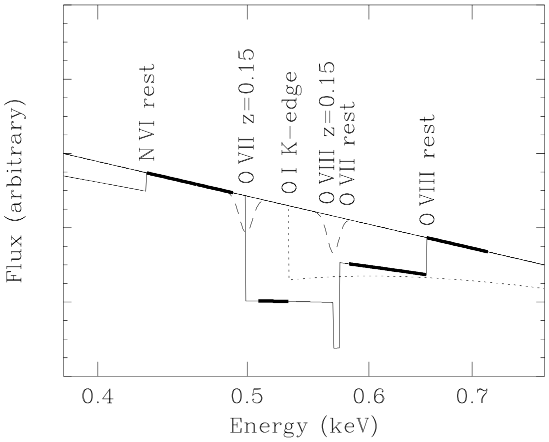

Flux (arbitrary)
N VI rest
O VII z=0.15
O I K−edge
O VIII z=0.15
O VII rest
O VIII rest
0.4
0.5
0.6
0.7
Energy (keV)

Fig. 13.—

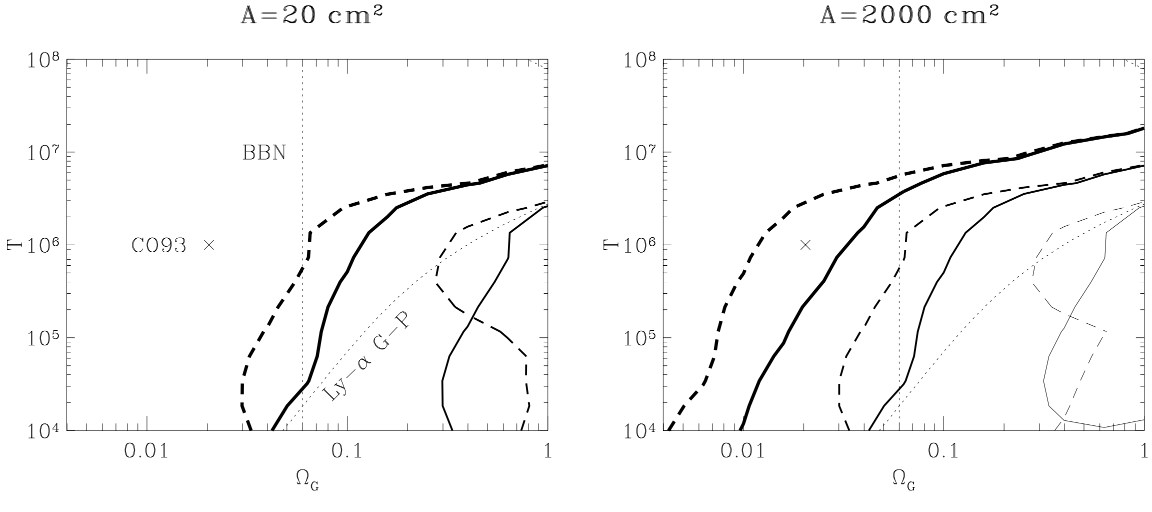

A=20 cm²
A=2000 cm²
T
10^8
10^7
10^6
10^5
10^4
BBN
CO93
Ly−α G−P
0.01
0.1
1
Ω_G

Fig. 14.—